



**HAL**  
open science

## Atmospheric Nitrous Acid Measurement in the French Landes Forest

Xinke Wang, Dandan Li, Pierre-Marie Flaud, Haiyan Li, Sebastien Perrier, Eric Villenave, Sebastien Dusanter, Alexandre Tomas, Emilie Perraudin, Christian George, et al.

► **To cite this version:**

Xinke Wang, Dandan Li, Pierre-Marie Flaud, Haiyan Li, Sebastien Perrier, et al.. Atmospheric Nitrous Acid Measurement in the French Landes Forest. ACS Earth and Space Chemistry, 2022, 6 (1), pp.25-33. 10.1021/acsearthspacechem.1c00231 . hal-03525996

**HAL Id: hal-03525996**

**<https://hal.science/hal-03525996>**

Submitted on 12 Oct 2023

**HAL** is a multi-disciplinary open access archive for the deposit and dissemination of scientific research documents, whether they are published or not. The documents may come from teaching and research institutions in France or abroad, or from public or private research centers.

L'archive ouverte pluridisciplinaire **HAL**, est destinée au dépôt et à la diffusion de documents scientifiques de niveau recherche, publiés ou non, émanant des établissements d'enseignement et de recherche français ou étrangers, des laboratoires publics ou privés.

# Atmospheric nitrous acid measurement in the French Landes forest

Xinke Wang,<sup>†</sup> Dandan Li,<sup>†</sup> Pierre-Marie Flaud,<sup>‡</sup> Haiyan Li,<sup>§</sup> Sebastien Perrier,<sup>†</sup> Eric Villenave,<sup>‡</sup>  
Sebastien Dusanter,<sup>||</sup> Alexandre Tomas,<sup>||</sup> Emilie Perraudin,<sup>‡,\*</sup> Christian George,<sup>†,\*</sup> Matthieu  
Riva<sup>†,\*</sup>

<sup>†</sup>Univ Lyon, Université Claude Bernard Lyon 1, CNRS, IRCELYON, F-69626, Villeurbanne, France.

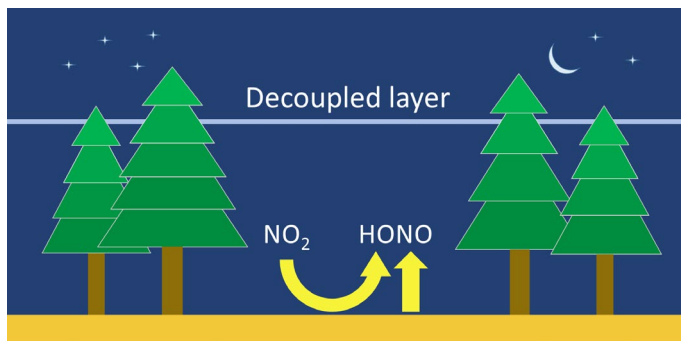
<sup>‡</sup>Univ. Bordeaux, EPOC, UMR 5805, F-33405 Talence Cedex, France

<sup>§</sup>School of Civil and Environmental Engineering, Harbin Institute of Technology, Shenzhen, 518055, China

<sup>||</sup>IMT Lille Douai, Institut Mines-Télécom, Univ. Lille, Center for Energy and Environment, F-59000, Lille, France

\*To whom correspondence should be addressed. Email: [christian.george@ircelyon.univ-lyon1.fr](mailto:christian.george@ircelyon.univ-lyon1.fr),  
[matthieu.riva@ircelyon.univ-lyon1.fr](mailto:matthieu.riva@ircelyon.univ-lyon1.fr), [emilie.perraudin@u-bordeaux.fr](mailto:emilie.perraudin@u-bordeaux.fr)

## TOC Figure



16 **ABSTRACT**

17 Nitrous acid (HONO) is a major hydroxyl radical (OH) source, which plays a central role in  
18 atmospheric chemistry. In this study, continuous measurements of HONO and other related  
19 parameters were conducted from 5<sup>th</sup> to 25<sup>th</sup> July 2018 in the French Landes forest. The mean  
20 daytime and nighttime HONO concentrations were 60 ppt and 139 ppt, respectively, whilst the  
21 mean daily OH production rate from HONO photolysis below the forest canopy was estimated to  
22 be  $7.6 \times 10^4$  molecules  $\text{cm}^{-3} \text{s}^{-1}$ , much less than those from ozone ( $\text{O}_3$ ) photolysis in the presence  
23 of water vapor ( $3.1 \times 10^5$  molecules  $\text{cm}^{-3} \text{s}^{-1}$ ) and alkene ozonolysis ( $4.4 \times 10^6$  molecules  $\text{cm}^{-3} \text{s}^{-1}$ ).  
24 Interestingly, the HONO levels were daily peaking between 18:00 to 24:00, that cannot be  
25 explained by the known chemical formation pathways. Analysis of collocated measurements  
26 suggested that the accumulation of HONO during the evening might be explained by  
27 micrometeorological processes. Hence creation of a stable decoupled layer retaining the HONO  
28 emission from the soil was associated with the formation of a convective decoupled layer.  
29 Increasing relative humidity within this period enhanced HONO gaseous deposition leading to its  
30 fast depletion.

31 **KEYWORDS**

32 nitrous acid, Landes forest, atmospheric photochemistry, micrometeorological process, decoupled  
33 layer, soil emission

34

## 35 **Introduction**

36 Nitrous acid (HONO) plays an important role in atmospheric photochemistry due to its fast  
37 photolysis yielding hydroxyl radicals (OH) and nitric oxide (NO), both of which contribute to the  
38 ground-level ozone (O<sub>3</sub>) and aerosol production.<sup>1-4</sup> Many field and modeling studies have shown  
39 that HONO photolysis can contribute to 25-56% of OH radical production in the daytime,<sup>5-7</sup> even  
40 reaching up to 80% in the early morning.<sup>8</sup> Despite the significance of HONO to atmospheric  
41 chemistry, a molecular-level understanding of its sources remains unclear.<sup>6,9</sup>

42 During the past decades, a large number of ambient HONO measurements have been  
43 conducted at various sites including rural, suburban, urban, forest, mountain, ocean and even in  
44 polar regions, showing that HONO concentration ranges from several ppt to more than 10 ppb.<sup>6,10-</sup>  
45 <sup>18</sup> Anthropogenic direct emissions such as vehicle exhaust with emission ratios of HONO/NO<sub>x</sub>  
46 ranging from 0.3% to 1.6% and natural sources including soil emission are regarded as important  
47 HONO sources for urban/suburban, and rural/forest regions, respectively.<sup>19-21</sup> The study of Su et  
48 al.<sup>19</sup> showed that HONO can be released from nitrite degradation present in the soil and might  
49 strongly increase globally due to the enhanced fertilizer use and soil acidification. However, soil  
50 biological activity has been recently suggested as the most important HONO source from soil  
51 emission.<sup>22</sup> This process can release HONO in greater quantities than from the acid-base and  
52 Henry's law equilibria of the aqueous phase in soil, but its production is influenced by the soil  
53 temperature and water content as a result of their influence on microbial activity.

54 In addition to primary emissions, the atmospheric secondary reactions including gas phase  
55 reaction of NO with OH radicals<sup>9,23</sup> and heterogeneous reactions of NO<sub>2</sub> on various surfaces such  
56 as ground, leaf, etc., are also suggested to significantly contribute to HONO formation.<sup>2</sup> In recent  
57 years, many laboratory studies have shown that photolysis of nitric acid (HNO<sub>3</sub>) and nitrate ions

58 ( $\text{NO}_3^-$ ) can be an important daytime source of HONO.<sup>24-26</sup> In addition, HONO production from  
59 aqueous nitrate photolysis can be enhanced by dissolved aliphatic organic matter due to the reaction  
60 of  $\text{O}_2^-$  with  $\text{NO}_x$  producing nitrite ( $\text{NO}_2^-$ ).<sup>27</sup> Moreover, the photosensitized conversion of  $\text{NO}_2$  on  
61 surfaces was also proved to be an efficient HONO formation pathway,<sup>28,29</sup> whilst the ozonolysis  
62 and photolysis of organic nitrogen substances, such as neonicotinoid nitenpyram ozonolysis<sup>30</sup>  
63 and ortho-nitrophenols<sup>31</sup> and nitrotyrosine photolysis,<sup>32</sup> are also suggested to be responsible for the  
64 formation of HONO. These findings are helpful to fill the gaps between the field observations and  
65 numerical models. However, the sources and fate of HONO in ambient conditions remain still  
66 unclear.<sup>9</sup>

67 In addition to these direct emission and formation pathways, the local micrometeorological  
68 processes can also significantly influence the primary pollutant concentrations and should not be  
69 neglected. As an example, it has been recently reported that the formation of a shallow decoupled  
70 layer below the canopy, can lead to a significant increase of monoterpenes and monoterpene  
71 oxidation products near ground level in the Finnish boreal forest<sup>33</sup> and the French Landes forest.<sup>34</sup>

72 This work aims to contribute to unravel biological, chemical, physical and  
73 micrometeorological processes on HONO sources and sinks in the context of a forested site  
74 characterized by high levels of biogenic volatile organic compounds (BVOCs) and weakly  
75 influenced by anthropogenic emissions (i.e., low  $\text{NO}_x$  air masses). Measurements of atmospheric  
76 HONO as well as meteorological parameters, trace gases, and volatile organic compounds (VOCs)  
77 were performed in a maritime pine forest located in the French Landes (southwestern part of  
78 France), previously reported as a site highlighting high monoterpene concentrations.<sup>35,36</sup> Very  
79 surprisingly, a daily high HONO peak ranging from 18:00 to midnight was observed. The  
80 contribution of HONO photolysis to the primary OH production was evaluated and compared to

81 those of O<sub>3</sub> photolysis and reaction of the O(<sup>1</sup>D) product with water vapor as well as alkene  
82 ozonolysis. Finally, a HONO budget including soil emission, chemical formation and loss  
83 pathways as well as local micrometeorological processes was estimated and analyzed for the  
84 summer of 2018.

## 85 **Experimental section**

86 **Site description.** The measurements presented in this study were performed as part of the  
87 CERVOLAND (Characterization of Emissions and Reactivity of Volatile Organic Compounds in  
88 the Landes forest) campaign and conducted from 5<sup>th</sup> to 25<sup>th</sup> July 2018. The measurement site was  
89 located next to the European Integrated Carbon Observation System (ICOS) station at Bilos in the  
90 Landes forest (44°29'39.69" N, 0°57'21.75" W), which is around 40 km far from the nearest urban  
91 area of the Bordeaux metropole and 25 km from the North Atlantic Oceanic. More descriptions  
92 about the site were given in previous studies.<sup>35,37,38</sup> Briefly, this field site is mainly covered by  
93 maritime pine trees (*Pinus pinaster* Aiton) and weakly influenced by anthropogenic pollution. It is  
94 characterized by very high levels of biogenic VOCs (up to 20 ppb for the total monoterpene  
95 concentration)<sup>39,36</sup> and the soil is a sandy acidic hydromorphic podzol with a discontinuous layer  
96 of iron hard pan at a 75 cm depth.<sup>34</sup>

97 **Measurement techniques.** Atmospheric HONO was measured by a commercial long path  
98 absorption photometer instrument (QUMA, Model LOPAP-03). A detailed description of the  
99 LOPAP instrument can be found elsewhere.<sup>27,40</sup> In brief, the sampling stripping coil (at 4 m above  
100 the ground level (a.g.l.)) was kept at a constant temperature of 15°C and consists of two channels:  
101 channel 1 uptakes HONO and a small fraction of interfering species, while the interfering species  
102 are quantified by channel 2.<sup>41</sup> The ambient air sampling flow rate and peristaltic pump velocity

103 were set to  $1.1 \text{ L min}^{-1}$  and 10 revolutions per minute, with a HONO collection efficiency of 99.9%  
104 and an uncertainty of 10%. The LOPAP was calibrated by a known concentration nitrite ( $\text{NO}_2^-$ ,  
105 Titrisol,  $1000 \text{ mg L}^{-1} \text{ NO}_2^-$  in water) solution every 4 days, whilst zero measurements were  
106 conducted every 8 hours by injecting pure  $\text{N}_2$ . Detection limit of the LOPAP was estimated to be  
107  $0.3 \text{ ppt}$  (i.e., 2 times noise of zero measurements). Then, HONO concentration was obtained by  
108 subtracting the calibrated signal of channel 2 from channel 1 with a time resolution of 30 s.

109 In addition, the Vocus proton-transfer-reaction mass spectrometry (PTR-MS), with a high  
110 time response and sensitivity (detection limit  $< 1 \text{ ppt}$ ), was used to measure VOCs during this field  
111 campaign. More descriptions about the setup and the results of Vocus PTR-MS were reported  
112 elsewhere.<sup>36,42</sup> Additionally, the photolysis frequencies of  $\text{NO}_2$  and  $\text{O}_3$  represented by  $J_{\text{NO}_2}$  and  $J_{\text{O}_3}$   
113 were quantified by a spectroradiometer (Meteorologie Consult GmbH 6007) in a clearing. The  
114 photolysis frequency of HONO ( $J_{\text{HONO}}$ ) was obtained by multiplying  $J_{\text{NO}_2}$  by the ratio of calculated  
115  $J_{\text{HONO}}$  and  $J_{\text{NO}_2}$  based on the NCAR Tropospheric Ultraviolet and Visible (TUV) model.<sup>43,44</sup>  $\text{NO}_x$   
116 and ozone ( $\text{O}_3$ ) concentrations were measured at 4 m a.g.l. by chemiluminescence and UV  
117 absorption analyzers, respectively, both of which have a detection limit of  $0.5 \text{ ppb}$ . The  
118 meteorological parameters such as temperature (T), relative humidity (RH), wind speed (WS),  
119 wind direction as well as  $\text{CO}_2$  concentrations at 0.46, 1.6, 3.4, 5.7, 8.5, 11.8, and 15.6 m a.g.l. were  
120 continuously monitored, while the solar radiation was measured at 15.6 m a.g.l. and measurement  
121 data were provided by the European Integrated Carbon Observation System (ICOS) station. All  
122 data are reported and discussed in Coordinated Universal Time (UTC) in this study, two hours later  
123 than local time.

124 **Parametrization of OH concentration.** The steady OH concentration ( $[\text{OH}]_{\text{ss}}$ ) could be estimated  
125 using Eq. 1, as in the study by Mermet et al.:<sup>37</sup>

126 
$$[OH]_{ss} = 1 \times 10^5 + \frac{Rad_t \times K_{a,t}}{1 \times 10^3} \times [[OH]_{max} - 1 \times 10^5] \quad (\text{Eq. 1})$$

127 Notably,  $1 \times 10^5$  molecules  $\text{cm}^{-3}$  was retained as a typical value for OH concentration in forest  
 128 environments at nighttime.<sup>45-49</sup> The  $Rad_t$  ( $\text{W m}^{-2}$ ) was the solar irradiation above the forest canopy  
 129 and  $K_{a,t}$  was the ratio between the solar irradiance values measured below and above the canopy as  
 130 previously proposed by Mermet et al.,<sup>37</sup> whilst  $1 \times 10^3 \text{ W m}^{-2}$  was the maximum of solar irradiation  
 131 during the field campaign. Besides,  $6 \times 10^6$  molecules  $\text{cm}^{-3}$  measured by Birmili et al.<sup>48</sup> and  $3 \times$   
 132  $10^6$  molecules  $\text{cm}^{-3}$  reported by Hens et al.<sup>45</sup> were used as the high and lower limits of  $[OH]_{max}$ ,  
 133 respectively.<sup>37</sup>

134 In addition, another empirical formula proposed by Ehhalt & Rohrer (2000)<sup>51</sup> was widely  
 135 used to estimate the  $[OH]_{ss}$  concentration in the daytime:<sup>15,44,52</sup>

136 
$$[OH]_{ss} = a(J_{O1D})^\alpha (J_{NO2})^\beta \frac{bNO_2+1}{cNO_2^2+dNO_2+1} \quad (\text{Eq. 2})$$

137  $(\alpha = 0.83, \beta = 0.19, a = 4.1 \times 10^9, b = 140, c = 0.41, \text{ and } d = 1.7)$

138 If alkene ozonolysis dominates the production of OH radicals, notably during nighttime,  $[OH]_{ss}$   
 139 concentration can be calculated using the following equation:<sup>36,53</sup>

140 
$$[OH]_{ss} = \frac{\sum k_{(O_3+VOC_i)} \alpha_i [O_3] [alkene_i]}{\sum k_{(OH+VOC_i)} [alkene_i] + k_{(OH+O_3)} [O_3]} \quad (\text{Eq. 3})$$

141 where  $k_{(O_3+VOC)}$  is the rate constant for the reaction of  $O_3$  with alkenes with an OH yield of  $\alpha$ ;  
 142  $k_{(OH+VOC)}$  and  $k_{(OH+O_3)}$  are the rate constants for OH reacting with alkenes and  $O_3$ , respectively. The  
 143 main alkenes are monoterpenes in the Landes forest region, but also consist of a small amount of  
 144 isoprene and sesquiterpenes (Figures S1-S2).<sup>36</sup> In addition, a previous field observation in 2017  
 145 summer on the same site showed that the identified species including  $\alpha$ -pinene,  $\beta$ -pinene, camphene,  
 146 sabinene, myrcene, 2-carene,  $\alpha$ -phellandrene,  $\Delta^3$ -carene, limonene, ocimene,  $\alpha$ -terpinene,  
 147 terpinolene account for  $\sim 80\%$  of the total monoterpene concentrations, whilst  $\beta$ -caryophyllene

148 represents ~40% of the total sesquiterpenes and ~90% of total sesquiterpene reactivity.<sup>37</sup> Therefore,  
149 these identified species including their accounted percentages were selected for the calculations Eq.  
150 3, whilst their reaction rate constants with OH radicals and O<sub>3</sub> as well as their corresponding OH  
151 radical production yields were taken from previous studies.<sup>54-56</sup> Notably, OH production produced  
152 by the reactions of hydroperoxyl radical (HO<sub>2</sub>) with NO or O<sub>3</sub> was neglected, since NO  
153 concentration was below the detection limit of NO<sub>x</sub> analyzer most of the time, and HO<sub>2</sub>  
154 concentration was not measured in this study.

## 155 **RESULTS AND DISCUSSION**

156 **Measurements of meteorological conditions and trace gases.** Figure 1 displays an overview of  
157 meteorological conditions (measured at 3.4 m a.g.l. except for solar radiation measured at 15.6 m  
158 a.g.l.) and the measured HONO, NO<sub>x</sub>, and O<sub>3</sub> concentrations, for which diel variation pattern was  
159 consistent during the campaign.<sup>35</sup> Except for some rainy and cloudy days (i.e., 6<sup>th</sup>, 21<sup>st</sup>, and 22<sup>nd</sup>  
160 July), the weather remained sunny with strong solar irradiation, indicating favorable conditions for  
161 intense photochemical activities. The air masses within the forest canopy were relatively stable,  
162 with wind speed < 1 m s<sup>-1</sup>, suggesting a major influence of local emissions. The ambient  
163 temperature ranged from 11 °C to 35 °C with a mean value (± standard deviation) of 22 ± 6 °C and  
164 an average RH of 74 ± 21 %. Figure 1C shows that the average concentration of NO<sub>2</sub> was 1.6 ± 0.9  
165 ppb, while the concentration of NO was below the detection limit (i.e., < 0.5 ppb) most of the time,  
166 but showing a peak in the morning, with a maximum value of 5.6 ppb at 5:00 on 10<sup>th</sup> July. O<sub>3</sub>  
167 concentration appeared with a mean value of 28 ± 19 ppb, with an average maximum of 49 ppb at  
168 12:00 (Figure 2). The HONO concentration ranged from 4 ppt to 1.1 ppb, with a mean value of 96  
169 ± 107 ppt, which is slightly higher than typical values of 30 to 90 ppt previously observed in forest  
170 environments.<sup>10,17,57,58</sup>

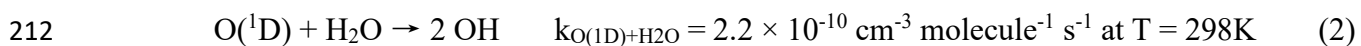
171 The diel profiles of meteorological conditions and trace gases are depicted in Figure 2, all  
172 of which showing clear diurnal variations. The CO<sub>2</sub> concentrations measured at different heights  
173 from 0.46 m a.g.l. to 15.6 m a.g.l. was used as a proxy to estimate the decoupled layer height  
174 (DLH).<sup>33</sup> The temperature, O<sub>3</sub> concentration and photolysis frequencies (i.e., J<sub>O<sub>3</sub></sub>, J<sub>NO<sub>2</sub></sub>, and J<sub>HONO</sub>)  
175 followed the pattern of the solar irradiation, while the RH and NO<sub>2</sub> concentrations exhibited  
176 opposite diel profiles. The mean NO<sub>2</sub> concentration started to increase from 0.9 ± 0.14 ppb at 14:00  
177 to 2.3 ± 1.3 ppb at 21:00, and stayed constant during the night. Consistent with the increase of NO<sub>2</sub>  
178 photolysis rate (Figure 2F) and the expansion of boundary layer height in the early morning, the  
179 concentration of NO<sub>2</sub> quickly declined. The average HONO concentrations in the daytime (UTC  
180 time, 7:00-19:00) and nighttime (UTC time, 20:00-next day 6:00) were 60 ± 32 ppt and 139 ± 72  
181 ppt, respectively. HONO measurements in the Finnish boreal forest also showed higher HONO  
182 concentrations at night,<sup>57</sup> while several other forest measurements exhibited the opposed trend due  
183 to unknown daytime HONO sources.<sup>10,17,59</sup> Interestingly, the mean HONO concentration quickly  
184 rose in the evening from 53 ± 29 ppt at 18:00 to 300 ± 209 ppt at 20:00 (Figure 2D), and the fastest  
185 increasing case was on 14<sup>th</sup> July, where the HONO concentration increased from 94 ppt to 1.1 ppb  
186 within 2 hours (Figure 1D). It is worth pointing out that such a fast rise has not yet been reported  
187 from previous HONO measurements.<sup>10,17,57,59</sup>

### 188 **Impact of HONO and O<sub>3</sub> photolysis and alkene ozonolysis on the primary OH production.**

189 Firstly, as shown in Figure 3A, the low and high [OH]<sub>ss</sub> concentrations calculated by Eq.1 are in  
190 the ranges of 1-10 × 10<sup>5</sup> molecules cm<sup>-3</sup> and 1-20 × 10<sup>5</sup> molecules cm<sup>-3</sup>, with the average values of  
191 2.9 × 10<sup>5</sup> molecules cm<sup>-3</sup> and 4.8 × 10<sup>5</sup> molecules cm<sup>-3</sup>, respectively. The maximum concentration  
192 of [OH]<sub>ss</sub> is shown at 11:00 owing to the strongest solar irradiation within the forest canopy,  
193 consistent with the maximum J<sub>NO<sub>2</sub></sub>, J<sub>HONO</sub> and J<sub>O<sub>3</sub></sub> (Figures 2E and 2F). Notably, all photolysis

194 frequencies below the forest canopy were calculated by the measured ones multiplying  $K_{a,t}$  (i.e.,  
 195 the ratio between the solar irradiance values measured below and above the canopy). Similarly, the  
 196  $[OH]_{ss}$  expressed by the  $NO_2$  concentrations and photolysis frequencies of  $O_3$  and  $NO_2$  (i.e.,  
 197 calculated by Eq. 2) also showed the maxima at 11:00, with a concentration of  $2.4 \times 10^6$  molecules  
 198  $cm^{-3}$ . It is worth noting that solar irradiation under the forest canopy was weak (Figure 2F) in the  
 199 time period of 17:00 to the next day 9:00, both of which suggesting that alkene ozonolysis might  
 200 have been the main source of OH radicals. Therefore,  $[OH]_{ss}$  is calculated by means of Eq. 3,  
 201 considering the competition between OH production and removal processes leading to the  $[OH]_{ss}$   
 202 formation. Different to the result calculated by Eq. 1, a greater  $[OH]_{ss}$  concentration in the range  
 203 of  $4-8 \times 10^5$  molecules  $cm^{-3}$  was observed during the time period from 17:00 to 24:00, that results  
 204 from the subsequent monoterpene ozonolysis. As a result, the average  $[OH]_{ss}$  concentration ( $7.4 \times$   
 205  $10^5$  molecule  $cm^{-3}$ ) calculated by Eqs. 2-3 is higher than those (low average value:  $2.9 \times 10^5$   
 206 molecule  $cm^{-3}$ , high average value:  $4.8 \times 10^5$  molecule  $cm^{-3}$ ) by Eq. 1.

207 It has been widely accepted that HONO photolysis is an important source of OH radicals  
 208 in the atmosphere, especially in urban and suburban regions.<sup>5,52,60</sup> In addition,  $O_3$  photolysis in the  
 209 presence of water vapor is the most important source of OH radicals globally (reactions 1-3) during  
 210 daytime.<sup>61</sup>



214 where M is  $N_2$  or  $O_2$ .

215 Then we compared the OH production rates from the photolysis of HONO and  $O_3$ , and alkene  
 216 ozonolysis. While considered here as the main OH production pathways yet some others such as

217 aldehyde photolysis or  $\text{RC}(\text{O})\text{O}_2$  with  $\text{HO}_2$  reaction may also contribute.<sup>62</sup> The OH production rates  
 218 from HONO photolysis ( $P_{\text{OH}}(\text{HONO})$ ),  $\text{O}_3$  photolysis in the presence of water vapor ( $P_{\text{OH}}(\text{O}^1\text{D})$ ),  
 219 and alkene ozonolysis ( $P_{\text{OH}}(\text{alkene ozonolysis})$ ) were calculated using equations 4-6,  
 220 respectively:<sup>52,54,61</sup>

$$221 \quad P_{\text{OH}}(\text{HONO}) = J_{\text{HONO}}[\text{HONO}] \quad (\text{Eq. 4})$$

$$222 \quad P_{\text{OH}}(\text{O}^1\text{D}) = \frac{2J(\text{O}^1\text{D})[\text{O}_3]k_{\text{O}^1\text{D}+\text{H}_2\text{O}}[\text{H}_2\text{O}]}{k_{\text{O}^1\text{D}+\text{H}_2\text{O}}[\text{H}_2\text{O}] + k_{\text{O}^1\text{D}+\text{M}}[\text{M}]} \quad (\text{Eq. 5})$$

$$223 \quad P_{\text{OH}}(\text{alkene ozonolysis}) = \sum k_{\text{O}_3+\text{alkene}_i} \alpha_i [\text{alkene}_i][\text{O}_3] \quad (\text{Eq. 6})$$

224 As depicted in Figure 3B,  $P_{\text{OH}}(\text{O}^1\text{D})$  showed a maximum value of  $1.6 \times 10^6$  molecules  $\text{cm}^{-3}$   
 225  $\text{s}^{-1}$  at 11:00 and a daily average value of  $3.1 \times 10^5$  molecules  $\text{cm}^{-3} \text{s}^{-1}$ . However,  $P_{\text{OH}}(\text{HONO})$  was  
 226 much less, showing a maximum value of  $3.7 \times 10^5$  molecules  $\text{cm}^{-3} \text{s}^{-1}$  at 11:00 and a mean  
 227 production rate of  $7.6 \times 10^4$  molecules  $\text{cm}^{-3} \text{s}^{-1}$ , respectively. On the contrary, as shown in Figure  
 228 3B, alkene ozonolysis contributes significantly to the OH radical formation from 18:00 to 24:00  
 229 with a mean production rate of  $9.1 \times 10^6$  molecules  $\text{cm}^{-3} \text{s}^{-1}$ , therefore, showing a daily average  
 230 production rate of  $4.4 \times 10^6$  molecules  $\text{cm}^{-3} \text{s}^{-1}$ , higher than  $P_{\text{OH}}(\text{O}^1\text{D})$  and  $P_{\text{OH}}(\text{HONO})$ . However,  
 231 it should be noted that even if alkene ozonolysis contributed significantly to OH formation,  $[\text{OH}]_{\text{ss}}$   
 232 still stayed at a relatively low level as a result of an active OH chemistry during this period,  
 233 confirmed by the formation of alkene-derived oxygenated VOCs.<sup>36</sup> All in all, this result shows  $P_{\text{OH}}$   
 234 (HONO) was insignificant in this area, only accounting for 1.6% of total daily OH production rate  
 235 from these different formation pathways, probably due to the low concentration of HONO in the  
 236 daytime and relatively weak solar irradiation below the forest canopy compared to that above the  
 237 forest canopy.

238 **HONO budget analysis from 18:00 to 24:00.** As discussed above, surprisingly, a daily high but  
239 unexplained HONO peak was observed from 18:00 to 24:00. Therefore, to identify the potential  
240 sources, the HONO budget was investigated during this period. Because the photolysis frequencies  
241 below the forest canopy were negligible (Figures 2E and 2F), the photochemical sources (i.e.,  
242  $\text{NO}_3^-/\text{HNO}_3$  photolysis, photosensitized oxidation of  $\text{NO}_2$ , etc.) and photolysis of HONO were not  
243 considered. As a result, the main factors affecting the ambient HONO concentration from 18:00 to  
244 24:00 were summarized by Eq. 7:

$$245 \quad \frac{d[\text{HONO}]}{dt} = P_{\text{het}} + P_{\text{OH+NO}} + P_{\text{emis}} + P_{\text{unknown}} - L_{\text{dep}} - L_{\text{OH+HONO}} \quad (\text{Eq. 7})$$

246 where,  $d[\text{HONO}]/dt$  is the observed change rate of HONO concentration; HONO sources include  
247 heterogeneous conversion of  $\text{NO}_2$  to HONO ( $P_{\text{het}}$ ), gas-phase reaction of OH and NO ( $P_{\text{OH+NO}}$ ),  
248 direct emission ( $P_{\text{emis}}$ ) and unknown sources including some processes influencing HONO  
249 concentration ( $P_{\text{unknown}}$ ), while the loss pathways include dry deposition of HONO ( $L_{\text{dep}}$ ) and  
250 reaction between OH and HONO ( $L_{\text{OH+HONO}}$ ).

251 Figure 4 shows the average rates of  $P_{\text{OH+NO}}$ ,  $P_{\text{het}}$ ,  $L_{\text{OH+HONO}}$ ,  $L_{\text{dep}}$ , and the sum of  $P_{\text{emis}}$  and  
252  $P_{\text{unknown}}$  during the period of 18:00-24:00, and the details on their calculations were described in  
253 the Supplemental Materials Text S1. First, the  $L_{\text{OH+HONO}}$  and  $P_{\text{OH+NO}}$  rates were negligible  
254 compared to other formation and loss pathways. Both  $P_{\text{het}}$  and  $L_{\text{dep}}$  rates were influenced by the  
255 DLH, which was around 6 m from 18:00 to 24:00, based on the separation of vertical  $\text{CO}_2$   
256 concentrations (Figure 2A) and temperature inversion (Figure 5). Notably, DLH includes stable  
257 decoupled layer height (SDL) and convective decoupled layer height (CDL) in the present study.  
258 Although the adopted value of DLH can impact the rates of  $P_{\text{het}}$  and  $L_{\text{dep}}$ , their ratio (i.e.,  $P_{\text{het}}/L_{\text{dep}}$ )  
259 remained constant.  $P_{\text{emis}}$  was not available in this study, but the sum of  $P_{\text{emis}}$  and  $P_{\text{unknown}}$  were  
260 calculated based on the Eq. 7. As shown in Figure 4, the known HONO sources, i.e., gas phase

261 reaction of NO with OH radicals and heterogeneous conversion of NO<sub>2</sub> on surfaces, cannot explain  
262 the fast increase of HONO ( $0.7\text{-}1.0 \times 10^6$  molecules cm<sup>-3</sup> s<sup>-1</sup>) during the nightfall (Figure 2D).

263 Interestingly, there is a temperature inversion layer formed at the ground level (~ 6 m) at ~  
264 17:00 (Figure 5), caused likely by radiation cooling.<sup>63,64</sup> This temperature inversion can yield a  
265 stable decoupled layer (SDL) close to the ground and retain the emissions from the ground and the  
266 vegetation within this thin layer,<sup>33,65</sup> concomitantly to the rapid increases of HONO (Figure 2D),  
267 NO<sub>2</sub> (Figure 2C) and monoterpene concentrations (Figure S2). However, the NO concentration  
268 stayed low from 18:00 to 24:00 due to the rapid consumption by peroxy radicals formed from the  
269 terpene ozonolysis and O<sub>3</sub>, producing organic nitrates (see Figure S3)<sup>36</sup> and NO<sub>2</sub>,<sup>61</sup> respectively.  
270 However, HONO concentration did not increase significantly at 17:00, due to its remaining strong  
271 photolysis (Figure 2E). Oswald et al.<sup>22</sup> showed that HONO emissions from soils were greater when  
272 soil temperature increases (20-30 °C), but less as soil water content increases (> 10% of water  
273 holding capacity). In this study, the gaseous HONO level showed strong positive and negative  
274 correlations with the ambient temperature (Figure S4A) and RH (Figure S5A), respectively. This  
275 is suggesting that soil emission can be potentially an important HONO source within the Landes  
276 forest. For example, the highest HONO peak detected during the field campaign might be related  
277 to the relatively higher temperature and lower RH in the evening on July 14<sup>th</sup> (Figure 1). The  
278 exchange of NO<sub>x</sub> and HONO between the various surfaces present (such as vegetation cover) and  
279 the atmosphere may be bi-directional, which cannot be distinguished in this study.

280 Afterwards, a weak convective decoupled layer (CDL) was created at the ground level after  
281 20:00 and remained stable at 22:00 until 6:00 of the next day (Figures 5D and 5E). Notably, the  
282 correlation between HONO and temperature became weaker (Figure S4B) but HONO  
283 concentration still showed a strong negative correlation with ambient RH (Figure S5B), suggesting

284 that increasing RH likely enhanced the deposition loss of gaseous HONO in addition to its negative  
285 influence on HONO emission from soil. Therefore, both the created weak CDL at the ground level  
286 and the increasing RH (Figure 1B) probably led to the fast depletion of gaseous HONO from 20:00  
287 to 24:00 (Figure 2D). However, the NO<sub>2</sub> concentration stayed constant and NO concentration  
288 showed an increasing trend during the night, which were probably due to their deposition rate (i.e.,  
289 NO<sub>2</sub>,  $3-8 \times 10^{-3} \text{ m s}^{-1}$ ; NO,  $1-2 \times 10^{-3} \text{ m s}^{-1}$ )<sup>66</sup> lower than HONO ( $2 \times 10^{-2} \text{ m s}^{-1}$ ), and less active O<sub>3</sub>  
290 chemistry. Interestingly, many isoprene-, monoterpene-, and sesquiterpene-derived oxidation  
291 products also show a similar high peak during this period (Figure S6 and the study of Li et al.  
292 (2020)). This was caused by high concentrations of terpenes and O<sub>3</sub> within the SDL at the ground  
293 level during the period from 17:00 to 20:00. After 20:00, the created CDL started to enhance the  
294 dry deposition of these oxidation products, whilst O<sub>3</sub> concentration decreases fast, both of which  
295 caused the fast loss of these oxidation products. During the period from 00:00 to 7:00, the gaseous  
296 HONO concentration stayed constant, indicating the sinks and sources of HONO reached an  
297 equilibrium.

298 Notably, the slope fitted by the linear regression for HONO/NO<sub>2</sub> ratios against time was  
299 generally used as the conversion frequency of NO<sub>2</sub>-to-HONO ( $P_{\text{het}}$ ) during the  
300 nighttime.<sup>10,15,16,44,52,60,67,68</sup> However, sometimes the creation of a SDL at the ground level can  
301 efficiently promote the concentrations of primary pollutants including HONO after sunset, which  
302 will overestimate the heterogeneous conversion rate of NO<sub>2</sub>-to-HONO. Therefore, chemical  
303 formation pathways, direct emissions and meteorological processes should all be taken into  
304 consideration to better understand the variations of atmospheric species during field observations.

## 305 **CONCLUSION**

306 In the atmosphere, HONO is present at trace levels, typically up to a few ppb, but plays an important  
307 role in the tropospheric chemistry due to its photolysis, producing one of the major oxidants (i.e.,  
308 OH radicals).<sup>1-4</sup> In the present study, HONO as well as meteorological conditions and other  
309 measured trace gases showed regular variations during the campaign except for rainy days. The  
310 daily mean HONO concentration was  $96 \pm 107$  ppt and exhibited a large increase from 19:00 to  
311 22:00.

312 Terpene ozonolysis contributed significantly to OH radical formation with an average value  
313 of  $4.4 \times 10^6$  molecules  $\text{cm}^{-3} \text{s}^{-1}$ , higher than  $\text{O}_3$  photolysis in the presence of water vapor and HONO  
314 photolysis, due to the active alkene ozonolysis chemistry after sunset. However, the daily OH  
315 formation rate from HONO photolysis was only around  $7.6 \times 10^4$  molecules  $\text{cm}^{-3} \text{s}^{-1}$  as a result of  
316 low HONO concentrations and relative weak solar irradiation below the forest canopy.  
317 Interestingly, HONO peaked daily from 18:00-24:00, up to 1 ppb, which was not yet reported for  
318 forested environments and could not be explained by the usually reported chemical formation  
319 pathways. The creation of an SDL at the ground level retaining HONO produced from the soil  
320 within the thick layer leads to a fast HONO increase. Afterwards, both the created CDL and  
321 increasing RH enhanced HONO deposition resulting in its fast loss. Overall, the local  
322 meteorological conditions are highlighted in this work to be critical parameters to be taken into  
323 account as they significantly influence air pollutants at the ground level.

324

## 325 **Acknowledgments and Data**

326 The authors would like to thank the PRIMEQUAL programme for financial support (ADEME,  
327 convention #1662C0024). This study has also been carried out with financial support from the

328 French National Research Agency (ANR) in the frame of the Investments for the future Programme,  
329 within the Cluster of Excellence COTE (ANR-10-LABX-45) of the University of Bordeaux.  
330 Special thanks to Dr Christophe Chipeaux and Dr Denis Loustau (ISPA-INRAE) for their precious  
331 help in providing meteorological data from the ICOS station facility. We are also grateful to Prof.  
332 Jörg Kleffmann (Bergische Universität Wuppertal) for the help during the CERVOLAND  
333 campaign.

### 334 References

- 335 (1) Alicke, B., Platt U., S. J. Impact of Nitrous Acid Photolysis on the Total Hydroxyl Radical Budget  
336 during the Limitation of Oxidant Production/Pianura Padana Produzione Di Ozono Study in Milan.  
337 *J. Geophys. Res.* **2002**, *107* (D22), 8196. <https://doi.org/10.1029/2000JD000075>.
- 338 (2) Finlayson-Pitts, B. J.; Wingen, L. M.; Sumner, A. L.; Syomin, D.; Ramazan, K. A. The  
339 Heterogeneous Hydrolysis of NO<sub>2</sub> in Laboratory Systems and in Outdoor and Indoor  
340 Atmospheres: An Integrated Mechanism. *Phys. Chem. Chem. Phys.* **2003**, *5* (2), 223–242.  
341 <https://doi.org/10.1039/b208564j>.
- 342 (3) Harris, G. W.; Carter, W. P. L.; Winer, A. M.; Pitts, J. N.; Platt, U.; Perner, D. Observations of  
343 Nitrous Acid in the Los Angeles Atmosphere and Implications for Predictions of Ozone-Precursor  
344 Relationships. *Environ. Sci. Technol.* **1982**, *16* (7), 414–419. <https://doi.org/10.1021/es00101a009>.
- 345 (4) Xue, L.; Gu, R.; Wang, T.; Wang, X.; Saunders, S.; Blake, D.; Louie, P. K. K.; Luk, C. W. Y.;  
346 Simpson, I.; Xu, Z.; Wang, Z.; Gao, Y.; Lee, S.; Mellouki, A.; Wang, W. Oxidative Capacity and  
347 Radical Chemistry in the Polluted Atmosphere of Hong Kong and Pearl River Delta Region:  
348 Analysis of a Severe Photochemical Smog Episode. *Atmos. Chem. Phys.* **2016**, *16* (15), 9891–  
349 9903. <https://doi.org/10.5194/acp-16-9891-2016>.
- 350 (5) Elshorbany, Y. F.; Kurtenbach, R.; Wiesen, P.; Lissi, E.; Rubio, M.; Villena, G.; Gramsch, E.;  
351 Rickard, A. R.; Pilling, M. J.; Kleffmann, J. Oxidation Capacity of the City Air of Santiago, Chile.  
352 *Atmos. Chem. Phys.* **2009**, *9* (6), 2257–2273. <https://doi.org/10.5194/acp-9-2257-2009>.
- 353 (6) Kleffmann, J.; Gavriloaiei, T.; Hofzumahaus, A.; Holland, F.; Koppmann, R.; Rupp, L.; Schlosser,  
354 E.; Siese, M.; Wahner, A. Daytime Formation of Nitrous Acid: A Major Source of OH Radicals in  
355 a Forest. *Geophys. Res. Lett.* **2005**, *32* (5), 1–4. <https://doi.org/10.1029/2005GL022524>.
- 356 (7) Michoud, V.; Kukui, A.; Camredon, M.; Colomb, A.; Borbon, A.; Miet, K.; Aumont, B.;  
357 Beekmann, M.; Durand-Jolibois, R.; Perrier, S.; Zapf, P.; Siour, G.; Ait-Helal, W.; Locoge, N.;  
358 Sauvage, S.; Afif, C.; Gros, V.; Furger, M.; Ancellet, G.; Doussin, J. F. Radical Budget Analysis in  
359 a Suburban European Site during the MEGAPOLI Summer Field Campaign. *Atmos. Chem. Phys.*  
360 **2012**, *12* (24), 11951–11974. <https://doi.org/10.5194/acp-12-11951-2012>.
- 361 (8) Acker, K.; Febo, A.; Trick, S.; Perrino, C.; Bruno, P.; Wiesen, P.; Möller, D.; Wieprecht, W.; Auel,  
362 R.; Giusto, M.; Geyer, A.; Platt, U.; Allegrini, I. Nitrous Acid in the Urban Area of Rome. *Atmos.*  
363 *Environ.* **2006**, *40* (17), 3123–3133. <https://doi.org/10.1016/j.atmosenv.2006.01.028>.
- 364 (9) Lee, J. D.; Whalley, L. K.; Heard, D. E.; Stone, D.; Dunmore, R. E.; Hamilton, J. F.; Young, D. E.;  
365 Allan, J. D.; Laufs, S.; Kleffmann, J. Detailed Budget Analysis of HONO in Central London  
366 Reveals a Missing Daytime Source. *Atmos. Chem. Phys.* **2016**, *16* (5), 2747–2764.  
367 <https://doi.org/10.5194/acp-16-2747-2016>.
- 368 (10) Acker, K.; Möller, D. Atmospheric Variation of Nitrous Acid at Different Sites in Europe. *Environ.*

- 369 *Chem.* **2007**, *4* (4), 242–255. <https://doi.org/10.1071/EN07023>.
- 370 (11) Bernard, F.; Cazaunau, M.; Grosselin, B.; Zhou, B.; Zheng, J.; Liang, P.; Zhang, Y.; Ye, X.; Daële,  
371 V.; Mu, Y.; Zhang, R.; Chen, J.; Mellouki, A. Measurements of Nitrous Acid (HONO) in Urban  
372 Area of Shanghai, China. *Environ. Sci. Pollut. Res.* **2016**, *23* (6), 5818–5829.  
373 <https://doi.org/10.1007/s11356-015-5797-4>.
- 374 (12) Li, X.; Brauers, T.; Häsel, R.; Bohn, B.; Fuchs, H.; Hofzumahaus, A.; Holland, F.; Lou, S.; Lu,  
375 K. D.; Rohrer, F.; Hu, M.; Zeng, L. M.; Zhang, Y. H.; Garland, R. M.; Su, H.; Nowak, A.;  
376 Wiedensohler, A.; Takegawa, N.; Shao, M.; Wahner, A. Exploring the Atmospheric Chemistry of  
377 Nitrous Acid (HONO) at a Rural Site in Southern China. *Atmos. Chem. Phys.* **2012**, *12* (3), 1497–  
378 1513. <https://doi.org/10.5194/acp-12-1497-2012>.
- 379 (13) Su, H.; Cheng, Y. F.; Shao, M.; Gao, D. F.; Yu, Z. Y.; Zeng, L. M.; Slanina, J.; Zhang, Y. H.;  
380 Wiedensohler, A. Nitrous Acid (HONO) and Its Daytime Sources at a Rural Site during the 2004  
381 PRIDE-PRD Experiment in China. *J. Geophys. Res. Atmos.* **2008**, *113* (14), 1–9.  
382 <https://doi.org/10.1029/2007JD009060>.
- 383 (14) Su, H.; Cheng, Y. F.; Cheng, P.; Zhang, Y. H.; Dong, S.; Zeng, L. M.; Wang, X.; Slanina, J.; Shao,  
384 M.; Wiedensohler, A. Observation of Nighttime Nitrous Acid (HONO) Formation at a Non-Urban  
385 Site during PRIDE-PRD2004 in China. *Atmos. Environ.* **2008**, *42* (25), 6219–6232.  
386 <https://doi.org/10.1016/j.atmosenv.2008.04.006>.
- 387 (15) Wen, L.; Chen, T.; Zheng, P.; Wu, L.; Wang, X.; Mellouki, A.; Xue, L.; Wang, W. Nitrous Acid in  
388 Marine Boundary Layer over Eastern Bohai Sea, China: Characteristics, Sources, and Implications.  
389 *Sci. Total Environ.* **2019**, *670*, 282–291. <https://doi.org/10.1016/j.scitotenv.2019.03.225>.
- 390 (16) Zha, Q.; Xue, L.; Wang, T.; Xu, Z.; Yeung, C.; Louie, P. K. K.; Luk, C. W. Y. Large Conversion  
391 Rates of NO<sub>2</sub> to HNO<sub>2</sub> Observed in Air Masses from the South China Sea: Evidence of Strong  
392 Production at Sea Surface? *Geophys. Res. Lett.* **2014**, *41* (21), 7710–7715.  
393 <https://doi.org/10.1002/2014GL061429>.
- 394 (17) Zhang, N.; Zhou, X.; Bertman, S.; Tang, D.; Alaghmand, M.; Shepson, P. B.; Carroll, M. A.  
395 Measurements of Ambient HONO Concentrations and Vertical HONO Flux above a Northern  
396 Michigan Forest Canopy. *Atmos. Chem. Phys.* **2012**, *12* (17), 8285–8296.  
397 <https://doi.org/10.5194/acp-12-8285-2012>.
- 398 (18) Zhou, X.; Beine, H. J.; Honrath, R. E.; Fuentes, J. D.; Simpson, W.; Shepson, P. B.; Bottenheim, J.  
399 W. Snowpack Photochemical Production of HONO: A Major Source of OH in the Arctic  
400 Boundary Layer in Springtime. *Geophys. Res. Lett.* **2001**, *28* (21), 4087–4090.  
401 <https://doi.org/10.1029/2001GL013531>.
- 402 (19) Su, H.; Cheng, Y.; Oswald, R.; Behrendt, T.; Trebs, I.; Meixner, F. X.; Andreae, M. O.; Cheng, P.;  
403 Zhang, Y.; Poschl, U. Soil Nitrite as a Source of Atmospheric HONO and OH Radicals. *Science*  
404 *(80-. )*. **2011**, *333* (6049), 1616–1618. <https://doi.org/10.1126/science.1207687>.
- 405 (20) Kirchstetter, T. W.; Harley, R. A.; Littlejohn, D. Measurement of Nitrous Acid in Motor Vehicle  
406 Exhaust. *Environ. Sci. Technol.* **1996**, *30* (9), 2843–2849. <https://doi.org/10.1021/es960135y>.
- 407 (21) Xu, Z.; Wang, T.; Wu, J.; Xue, L.; Chan, J.; Zha, Q.; Zhou, S.; Louie, P. K. K.; Luk, C. W. Y.  
408 Nitrous Acid (HONO) in a Polluted Subtropical Atmosphere: Seasonal Variability, Direct Vehicle  
409 Emissions and Heterogeneous Production at Ground Surface. *Atmos. Environ.* **2015**, *106* (x), 100–  
410 109. <https://doi.org/10.1016/j.atmosenv.2015.01.061>.
- 411 (22) Oswald, R.; Behrendt, T.; Ermel, M.; Wu, D.; Su, H.; Cheng, Y.; Breuninger, C.; Moravek, A.;  
412 Mougin, E.; Delon, C.; Loubet, B.; Pommerening-Roser, A.; Sorgel, M.; Poschl, U.; Hoffmann, T.;  
413 Andreae, M. O.; Meixner, F. X.; Trebs, I. HONO Emissions from Soil Bacteria as a Major Source  
414 of Atmospheric Reactive Nitrogen. *Science (80-. )*. **2013**, *341* (6151), 1233–1235.  
415 <https://doi.org/10.1126/science.1242266>.
- 416 (23) Kleffmann, J. Daytime Sources of Nitrous Acid (HONO) in the Atmospheric Boundary Layer.  
417 *ChemPhysChem* **2007**, *8* (8), 1137–1144. <https://doi.org/10.1002/cphc.200700016>.
- 418 (24) Zhou, X.; Zhang, N.; Teravest, M.; Tang, D.; Hou, J.; Bertman, S.; Alaghmand, M.; Shepson, P.  
419 B.; Carroll, M. A.; Griffith, S.; Dusanter, S.; Stevens, P. S. Nitric Acid Photolysis on Forest

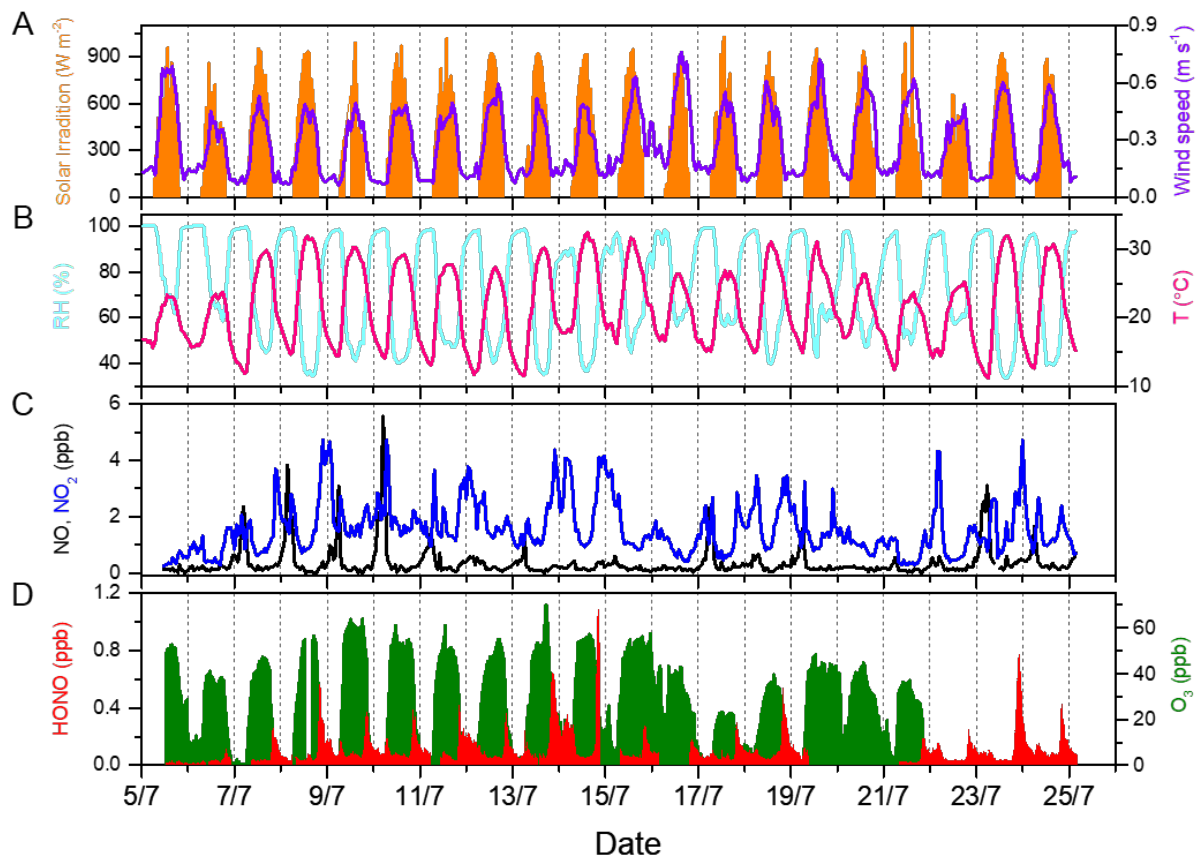
- 420 Canopy Surface as a Source for Tropospheric Nitrous Acid. *Nat. Geosci.* **2011**, *4* (7), 440–443.  
421 <https://doi.org/10.1038/ngeo1164>.
- 422 (25) Zhou, X.; Gao, H.; He, Y.; Huang, G.; Bertman, S. B.; Civerolo, K.; Schwab, J. Nitric Acid  
423 Photolysis on Surfaces in Low-NO<sub>x</sub> Environments: Significant Atmospheric Implications.  
424 *Geophys. Res. Lett.* **2003**, *30* (23), 10–13. <https://doi.org/10.1029/2003GL018620>.
- 425 (26) Scharko, N. K.; Berke, A. E.; Raff, J. D. Release of Nitrous Acid and Nitrogen Dioxide from  
426 Nitrate Photolysis in Acidic Aqueous Solutions. *Environ. Sci. Technol.* **2014**, *48* (20), 11991–  
427 12001. <https://doi.org/10.1021/es503088x>.
- 428 (27) Wang, X.; Dalton, E. Z.; Payne, Z. C.; Perrier, S.; Riva, M.; Raff, J. D.; George, C. Superoxide and  
429 Nitrous Acid Production from Nitrate Photolysis Is Enhanced by Dissolved Aliphatic Organic  
430 Matter. *Environ. Sci. Technol. Lett.* **2020**, [acs.estlett.0c00806](https://doi.org/10.1021/acs.estlett.0c00806).  
431 <https://doi.org/10.1021/acs.estlett.0c00806>.
- 432 (28) George, C.; Streckowski, R. S.; Kleffmann, J.; Stemmler, K.; Ammann, M. Photoenhanced Uptake  
433 of Gaseous NO<sub>2</sub> on Solid Organic Compounds: A Photochemical Source of HONO? *Faraday*  
434 *Discuss.* **2005**, *130* (2), 195. <https://doi.org/10.1039/b417888m>.
- 435 (29) Stemmler, K.; Ammann, M.; Donders, C.; Kleffmann, J.; George, C. Photosensitized Reduction of  
436 Nitrogen Dioxide on Humic Acid as a Source of Nitrous Acid. *Nature* **2006**, *440* (7081), 195–198.  
437 <https://doi.org/10.1038/nature04603>.
- 438 (30) Wang, W.; Ezell, M. J.; Lakey, P. S. J.; Aregahegn, K. Z.; Shiraiwa, M.; Finlayson-Pitts, B. J.  
439 Unexpected Formation of Oxygen-Free Products and Nitrous Acid from the Ozonolysis of the  
440 Neonicotinoid Nitenpyram. *Proc. Natl. Acad. Sci. U. S. A.* **2020**, *117* (21), 11321–11327.  
441 <https://doi.org/10.1073/pnas.2002397117>.
- 442 (31) Bejan, I.; Abd El Aal, Y.; Barnes, I.; Benter, T.; Bohn, B.; Wiesen, P.; Kleffmann, J. The  
443 Photolysis of Ortho-Nitrophenols: A New Gas Phase Source of HONO. *Phys. Chem. Chem. Phys.*  
444 **2006**, *8* (17), 2028–2035. <https://doi.org/10.1039/b516590c>.
- 445 (32) Meusel, H.; Elshorbany, Y.; Kuhn, U.; Bartels-Rausch, T.; Reinmuth-Selzle, K.; Kampf, C. J.; Li,  
446 G.; Wang, X.; Lelieveld, J.; Pöschl, U.; Hoffmann, T.; Su, H.; Ammann, M.; Cheng, Y. Light-  
447 Induced Protein Nitration and Degradation with HONO Emission. *Atmos. Chem. Phys.* **2017**, *17*  
448 (19), 11819–11833. <https://doi.org/10.5194/acp-17-11819-2017>.
- 449 (33) Zha, Q.; Yan, C.; Junninen, H.; Riva, M.; Sarnela, N.; Aalto, J.; Quéléver, L.; Schallhart, S.; Dada,  
450 L.; Heikkinen, L.; Peräkylä, O.; Zou, J.; Rose, C.; Wang, Y.; Mammarella, I.; Katul, G.; Vesala,  
451 T.; Worsnop, D. R.; Kulmala, M.; Petäjä, T.; Bianchi, F.; Ehn, M. Vertical Characterization of  
452 Highly Oxygenated Molecules (HOMs) below and above a Boreal Forest Canopy. *Atmos. Chem.*  
453 *Phys.* **2018**, *18* (23), 17437–17450. <https://doi.org/10.5194/acp-18-17437-2018>.
- 454 (34) Bsaibes, S.; Al Ajami, M.; Mermet, K.; Truong, F.; Batut, S.; Hecquet, C.; Dusanter, S.; Léonadis,  
455 T.; Sauvage, S.; Kammer, J.; Flaud, P. M.; Perraudin, E.; Villenave, E.; Locoge, N.; Gros, V.;  
456 Schoemaeker, C. Variability of Hydroxyl Radical (OH) Reactivity in the Landes Maritime Pine  
457 Forest: Results from the LANDEX Campaign 2017. *Atmos. Chem. Phys.* **2020**, *20* (3), 1277–1300.  
458 <https://doi.org/10.5194/acp-20-1277-2020>.
- 459 (35) Kammer, J.; Perraudin, E.; Flaud, P. M.; Lamaud, E.; Bonnefond, J. M.; Villenave, E. Observation  
460 of Nighttime New Particle Formation over the French Landes Forest. *Sci. Total Environ.* **2018**,  
461 *621*, 1084–1092. <https://doi.org/10.1016/j.scitotenv.2017.10.118>.
- 462 (36) Li, H.; Riva, M.; Rantala, P.; Heikkinen, L.; Daellenbach, K.; Krechmer, J. E.; Flaud, P.-M.;  
463 Worsnop, D.; Kulmala, M.; Villenave, E.; Perraudin, E.; Ehn, M.; Bianchi, F. Terpenes and Their  
464 Oxidation Products in the French Landes Forest: Insights from Vocus PTR-TOF Measurements.  
465 *Atmos. Chem. Phys.* **2020**, *20* (4), 1941–1959. <https://doi.org/10.5194/acp-20-1941-2020>.
- 466 (37) Mermet, K.; Perraudin, E.; Dusanter, S.; Sauvage, S.; Léonadis, T.; Flaud, P. M.; Bsaibes, S.;  
467 Kammer, J.; Michoud, V.; Gratien, A.; Cirtog, M.; Al Ajami, M.; Truong, F.; Batut, S.; Hecquet,  
468 C.; Doussin, J. F.; Schoemaeker, C.; Gros, V.; Locoge, N.; Villenave, E. Atmospheric Reactivity  
469 of Biogenic Volatile Organic Compounds in a Maritime Pine Forest during the LANDEX Episode  
470 1 Field Campaign. *Sci. Total Environ.* **2021**, *756*, 144129.

- 471 <https://doi.org/10.1016/j.scitotenv.2020.144129>.
- 472 (38) Kammer, J.; Flaud, P. M.; Chazeaubeny, A.; Ciuraru, R.; Le Menach, K.; Geneste, E.; Budzinski,  
473 H.; Bonnefond, J. M.; Lamaud, E.; Perraudin, E.; Villenave, E. Biogenic Volatile Organic  
474 Compounds (BVOCs) Reactivity Related to New Particle Formation (NPF) over the Landes  
475 Forest. *Atmos. Res.* **2020**, *237* (December 2019), 104869.  
476 <https://doi.org/10.1016/j.atmosres.2020.104869>.
- 477 (39) Mermet, K.; Sauvage, S.; Dusanter, S.; Salameh, T.; Léonardis, T.; Flaud, P. M.; Perraudin, E.;  
478 Villenave, E.; Locoge, N. Optimization of a Gas Chromatographic Unit for Measuring Biogenic  
479 Volatile Organic Compounds in Ambient Air. *Atmos. Meas. Tech.* **2019**, *12* (11), 6153–6171.  
480 <https://doi.org/10.5194/amt-12-6153-2019>.
- 481 (40) Heland, J.; Kleffmann, J.; Kurtenbach, R.; Wiesen, P. A New Instrument to Measure Gaseous  
482 Nitrous Acid (HONO) in the Atmosphere. *Environ. Sci. Technol.* **2001**, *35* (15), 3207–3212.  
483 <https://doi.org/10.1021/es000303t>.
- 484 (41) Kleffmann, J.; Wiesen, P. Technical Note: Quantification of Interferences of Wet Chemical HONO  
485 LOPAP Measurements under Simulated Polar Conditions. *Atmos. Chem. Phys.* **2008**, *8* (22), 6813–  
486 6822. <https://doi.org/10.5194/acp-8-6813-2008>.
- 487 (42) Li, H.; Canagaratna, M. R.; Riva, M.; Rantala, P.; Zhang, Y.; Thomas, S.; Heikkinen, L.; Flaud, P.  
488 M.; Villenave, E.; Perraudin, E.; Worsnop, D.; Kulmala, M.; Ehn, M.; Bianchi, F. Atmospheric  
489 Organic Vapors in Two European Pine Forests Measured by a Vocus PTR-TOF: Insights into  
490 Monoterpene and Sesquiterpene Oxidation Processes. *Atmos. Chem. Phys.* **2021**, *21* (5), 4123–  
491 4147. <https://doi.org/10.5194/acp-21-4123-2021>.
- 492 (43) Li, D.; Xue, L.; Wen, L.; Wang, X.; Chen, T.; Mellouki, A.; Chen, J.; Wang, W. Characteristics  
493 and Sources of Nitrous Acid in an Urban Atmosphere of Northern China: Results from 1-Yr  
494 Continuous Observations. *Atmos. Environ.* **2018**, *182* (March), 296–306.  
495 <https://doi.org/10.1016/j.atmosenv.2018.03.033>.
- 496 (44) Cui, L.; Li, R.; Fu, H.; Li, Q.; Zhang, L.; George, C.; Chen, J. Formation Features of Nitrous Acid  
497 in the Offshore Area of the East China Sea. *Sci. Total Environ.* **2019**, *682*, 138–150.  
498 <https://doi.org/10.1016/j.scitotenv.2019.05.004>.
- 499 (45) Hens, K.; Novelli, A.; Martinez, M.; Auld, J.; Axinte, R.; Bohn, B.; Fischer, H.; Keronen, P.;  
500 Kubistin, D.; Nölscher, A. C.; Oswald, R.; Paasonen, P.; Petäjä, T.; Regelin, E.; Sander, R.; Sinha,  
501 V.; Sipilä, M.; Taraborrelli, D.; Tatum Ernest, C.; Williams, J.; Lelieveld, J.; Harder, H.  
502 Observation and Modelling of HOx Radicals in a Boreal Forest. *Atmos. Chem. Phys.* **2014**, *14* (16),  
503 8723–8747. <https://doi.org/10.5194/acp-14-8723-2014>.
- 504 (46) Griffith, S. M.; Hansen, R. F.; Dusanter, S.; Stevens, P. S.; Alaghmand, M.; Bertman, S. B.;  
505 Carroll, M. A.; Erickson, M.; Galloway, M.; Grossberg, N.; Hottle, J.; Hou, J.; Jobson, B. T.;  
506 Kammrath, A.; Keutsch, F. N.; Lefer, B. L.; Mielke, L. H.; O'Brien, A.; Shepson, P. B.; Thurlow,  
507 M.; Wallace, W.; Zhang, N.; Zhou, X. L. OH and HO<sub>2</sub> Radical Chemistry during PROPHET 2008  
508 and CABINEX 2009 - Part 1: Measurements and Model Comparison. *Atmos. Chem. Phys.* **2013**,  
509 *13* (11), 5403–5423. <https://doi.org/10.5194/acp-13-5403-2013>.
- 510 (47) Petäjä, T.; Mauldin, R. L.; Kosciuch, E.; McGrath, J.; Nieminen, T.; Paasonen, P.; Boy, M.;  
511 Adamov, A.; Kotiaho, T.; Kulmala, M. Sulfuric Acid and OH Concentrations in a Boreal Forest  
512 Site. *Atmos. Chem. Phys.* **2009**, *9* (19), 7435–7448. <https://doi.org/10.5194/acp-9-7435-2009>.
- 513 (48) Birmili, W.; Berresheim, H.; Plass-Dülmer, C.; Elste, T.; Gilge, S.; Wiedensohler, A.; Uhrner, U.  
514 The Hohenpeissenberg Aerosol Formation Experiment (HAFEX): A Long-Term Study Including  
515 Size-Resolved Aerosol, H<sub>2</sub>SO<sub>4</sub>, OH, and Monoterpenes Measurements. *Atmos. Chem. Phys.* **2003**,  
516 *3* (2), 361–376. <https://doi.org/10.5194/acp-3-361-2003>.
- 517 (49) Berresheim, H.; Elste, T.; Plass-Dülmer, C.; Eisele, F. L.; Tanner, D. J. Chemical Ionization Mass  
518 Spectrometer for Long-Term Measurements of Atmospheric OH and H<sub>2</sub>SO<sub>4</sub>. *Int. J. Mass*  
519 *Spectrom.* **2000**, *202* (1–3), 91–109. [https://doi.org/10.1016/S1387-3806\(00\)00233-5](https://doi.org/10.1016/S1387-3806(00)00233-5).
- 520 (50) Ehhalt, D. H.; Rohrer, F. Dependence on Solar UV. **2000**, *105* (August 1994), 3565–3571.
- 521 (51) Ehhalt, D. H.; Rohrer, F. Dependence of the OH Concentration on Solar UV. *J. Geophys. Res.*

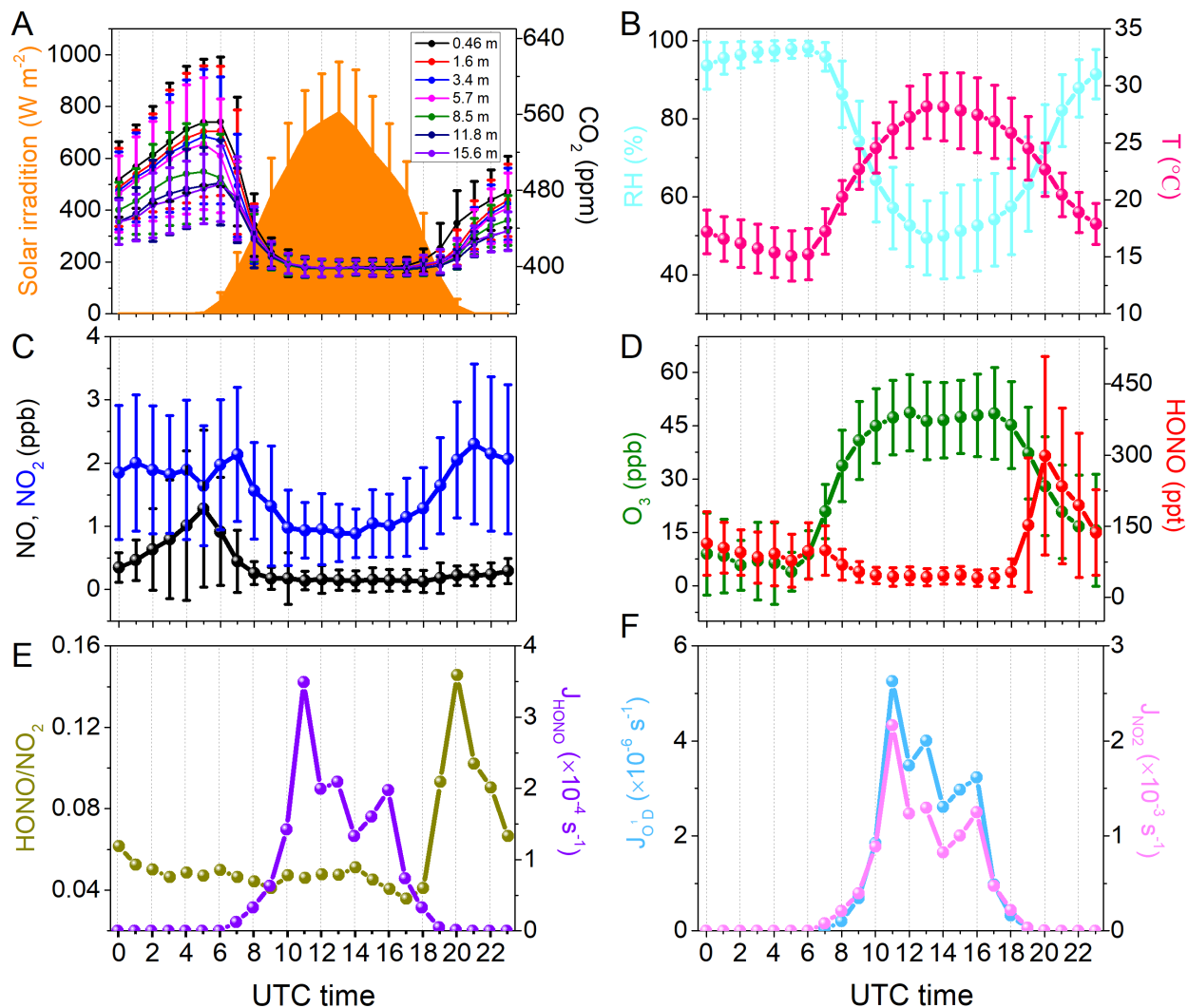
- 522 *Atmos.* **2000**, *105* (D3), 3565–3571. <https://doi.org/10.1029/1999JD901070>.
- 523 (52) Li, D.; Xue, L.; Wen, L.; Wang, X.; Chen, T.; Mellouki, A.; Chen, J.; Wang, W. Characteristics  
524 and Sources of Nitrous Acid in an Urban Atmosphere of Northern China: Results from 1-Yr  
525 Continuous Observations. *Atmos. Environ.* **2018**, *182* (July 2017), 296–306.  
526 <https://doi.org/10.1016/j.atmosenv.2018.03.033>.
- 527 (53) Dusanter, S.; Vimal, D.; Stevens, P. S. Technical Note: Measuring Tropospheric OH and HO<sub>2</sub> by  
528 Laser-Induced Fluorescence at Low Pressure. A Comparison of Calibration Techniques. *Atmos.*  
529 *Chem. Phys.* **2008**, *8* (2), 321–340. <https://doi.org/10.5194/acp-8-321-2008>.
- 530 (54) Aliche, B.; Geyer, A.; Hofzumahaus, A.; Holland, F.; Konrad, S.; Pätz, H. W.; Schäfer, J.; Stutz,  
531 J.; Volz-Thomas, A.; Platt, U. OH Formation by HONO Photolysis during the BERLIOZ  
532 Experiment. *J. Geophys. Res. D Atmos.* **2003**, *108* (4), 3–1. <https://doi.org/10.1029/2001jd000579>.
- 533 (55) Aschmann, S. M.; Arey, J.; Atkinson, R. OH Radical Formation from the Gas-Phase Reactions of  
534 O<sub>3</sub> with a Series of Terpenes. *Atmos. Environ.* **2002**, *36* (27), 4347–4355.  
535 [https://doi.org/10.1016/S1352-2310\(02\)00355-2](https://doi.org/10.1016/S1352-2310(02)00355-2).
- 536 (56) Winterhalter, R.; Herrmann, F.; Kanawati, B.; Nguyen, T. L.; Peeters, J.; Vereecken, L.; Moortgat,  
537 G. K. The Gas-Phase Ozonolysis of  $\beta$ -Caryophyllene (C<sub>15</sub>H<sub>24</sub>). Part I: An Experimental Study.  
538 *Phys. Chem. Chem. Phys.* **2009**, *11* (21), 4152–4172. <https://doi.org/10.1039/b817824k>.
- 539 (57) Oswald, R.; Ermel, M.; Hens, K.; Novelli, A.; Ouwensloot, H. G.; Paasonen, P.; Petäjä, T.; Sipilä,  
540 M.; Keronen, P.; Bäck, J.; Königstedt, R.; Hosaynali Beygi, Z.; Fischer, H.; Bohn, B.; Kubistin, D.;  
541 Harder, H.; Martinez, M.; Williams, J.; Hoffmann, T.; Trebs, I.; Sörgel, M. A Comparison of  
542 HONO Budgets for Two Measurement Heights at a Field Station within the Boreal Forest in  
543 Finland. *Atmos. Chem. Phys.* **2015**, *15* (2), 799–813. <https://doi.org/10.5194/acp-15-799-2015>.
- 544 (58) Ren, X.; Gao, H.; Zhou, X.; Crouse, J. D.; Wennberg, P. O.; Browne, E. C.; LaFranchi, B. W.;  
545 Cohen, R. C.; McKay, M.; Goldstein, A. H.; Mao, J. Measurement of Atmospheric Nitrous Acid at  
546 Bodgett Forest during BEARPEX2007. *Atmos. Chem. Phys.* **2010**, *10* (13), 6283–6294.  
547 <https://doi.org/10.5194/acp-10-6283-2010>.
- 548 (59) Acker, K.; Möller, D.; Wieprecht, W.; Meixner, F. X.; Bohn, B.; Gilge, S.; Plass-Dülmer, C.;  
549 Berresheim, H. Strong Daytime Production of OH from HNO<sub>2</sub> at a Rural Mountain Site. *Geophys.*  
550 *Res. Lett.* **2006**, *33* (2). <https://doi.org/10.1029/2005GL024643>.
- 551 (60) Hou, S.; Tong, S.; Ge, M.; An, J. Comparison of Atmospheric Nitrous Acid during Severe Haze  
552 and Clean Periods in Beijing, China. *Atmos. Environ.* **2016**, *124*, 199–206.  
553 <https://doi.org/10.1016/j.atmosenv.2015.06.023>.
- 554 (61) Atkinson, R.; Baulch, D. L.; Cox, R. A.; Crowley, J. N.; Hampson, R. F.; Hynes, R. G.; Jenkin, M.  
555 E.; Rossi, M. J.; Troe, J. Evaluated Kinetic and Photochemical Data for Atmospheric Chemistry:  
556 Volume I - Gas Phase Reactions of O<sub>x</sub>, HO<sub>x</sub>, NO<sub>x</sub> and SO<sub>x</sub> Species. *Atmos. Chem. Phys.* **2004**, *4*  
557 (6), 1461–1738. <https://doi.org/10.5194/acp-4-1461-2004>.
- 558 (62) Kleffmann, J.; Gavriloaiei, T.; Hofzumahaus, A.; Holland, F.; Koppmann, R.; Rupp, L.; Schlosser,  
559 E.; Siese, M.; Wahner, A. Daytime Formation of Nitrous Acid: A Major Source of OH Radicals in  
560 a Forest. *Geophys. Res. Lett.* **2005**, *32* (5), 1–4. <https://doi.org/10.1029/2005GL022524>.
- 561 (63) Fernando, H. J. S.; Weil, J. C. Whither the Stable Boundary Layer? *Bull. Am. Meteorol. Soc.* **2010**,  
562 *91* (11), 1475–1484. <https://doi.org/10.1175/2010BAMS2770.1>.
- 563 (64) Klein, P. M.; Hu, X. M.; Shapiro, A.; Xue, M. Linkages Between Boundary-Layer Structure and  
564 the Development of Nocturnal Low-Level Jets in Central Oklahoma. *Boundary-Layer Meteorol.*  
565 **2016**, *158* (3), 383–408. <https://doi.org/10.1007/s10546-015-0097-6>.
- 566 (65) Yuval; Levi, Y.; Dayan, U.; Levy, I.; Broday, D. M. On the Association between Characteristics of  
567 the Atmospheric Boundary Layer and Air Pollution Concentrations. *Atmos. Res.* **2020**, *231*  
568 (September 2019), 104675. <https://doi.org/10.1016/j.atmosres.2019.104675>.
- 569 (66) Judeikis, H. S.; Wren, A. G. Laboratory Measurements of NO and NO<sub>2</sub> Depositions onto Soil and  
570 Cement Surfaces. *Atmos. Environ.* **1978**, *12* (12), 2315–2319. [https://doi.org/10.1016/0004-6981\(78\)90272-X](https://doi.org/10.1016/0004-6981(78)90272-X).
- 571
- 572 (67) Huang, R. J.; Yang, L.; Cao, J.; Wang, Q.; Tie, X.; Ho, K. F.; Shen, Z.; Zhang, R.; Li, G.; Zhu, C.;

573 Zhang, N.; Dai, W.; Zhou, J.; Liu, S.; Chen, Y.; Chen, J.; O'Dowd, C. D. Concentration and  
574 Sources of Atmospheric Nitrous Acid (HONO) at an Urban Site in Western China. *Sci. Total*  
575 *Environ.* **2017**, *593–594*, 165–172. <https://doi.org/10.1016/j.scitotenv.2017.02.166>.  
576 (68) Kleffmann, J.; Kurtenbach, R.; Lörzer, J.; Wiesen, P.; Kalthoff, N.; Vogel, B.; Vogel, H. Measured  
577 and Simulated Vertical Profiles of Nitrous Acid - Part I: Field Measurements. *Atmos. Environ.*  
578 **2003**, *37* (21), 2949–2955. [https://doi.org/10.1016/S1352-2310\(03\)00242-5](https://doi.org/10.1016/S1352-2310(03)00242-5).  
579  
580

581 **Figures**



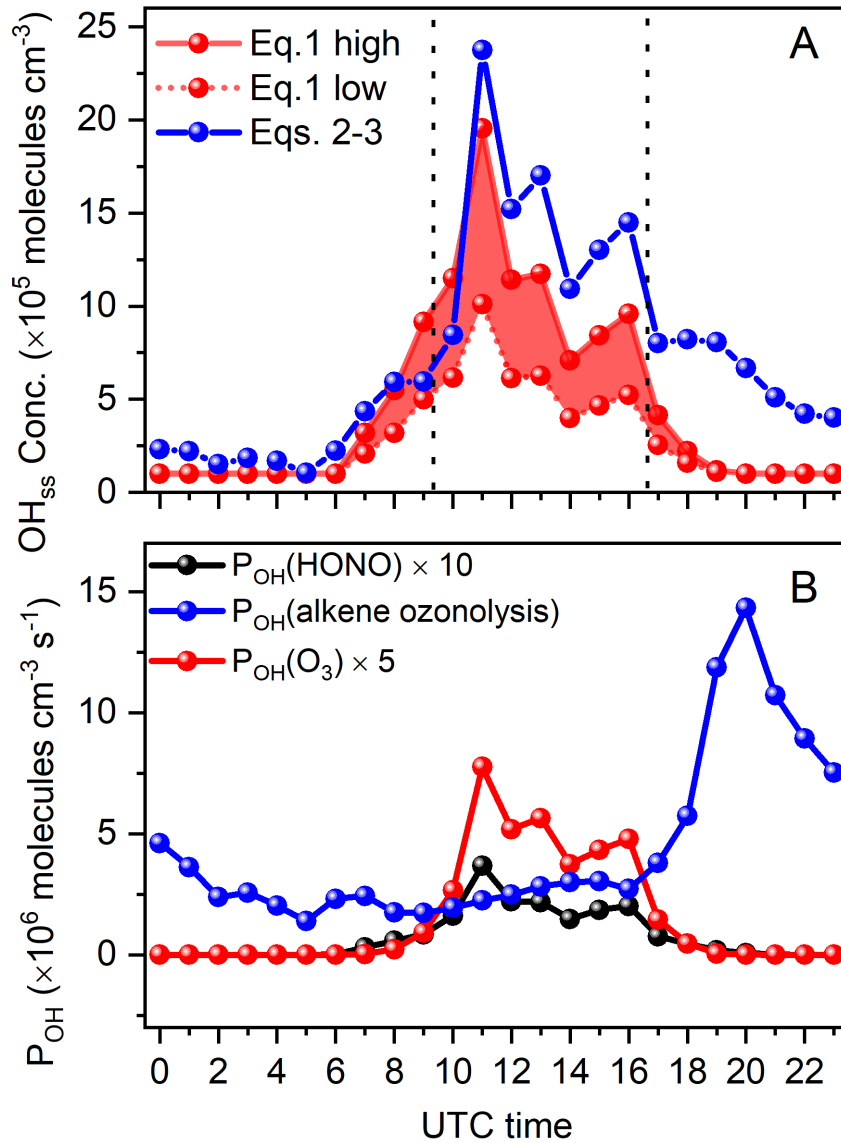
582  
583 Figure 1. Temporal variations of (A-B) meteorological parameters and measured (C) NO and NO<sub>2</sub>,  
584 (D) HONO and O<sub>3</sub> during the measurement period from 5<sup>th</sup> to 25<sup>th</sup> July, 2018.



585  
 586 Figure 2. Average diel variations of (A-B) meteorological parameters and CO<sub>2</sub> concentrations at  
 587 different heights and measured concentrations of (C) NO<sub>x</sub>, (D) HONO and O<sub>3</sub>, (E) HONO/NO<sub>2</sub>  
 588 and calculated J<sub>HONO</sub>, (F) J<sub>O1D</sub> and J<sub>NO2</sub> below the forest canopy during the measurement period.

589

590

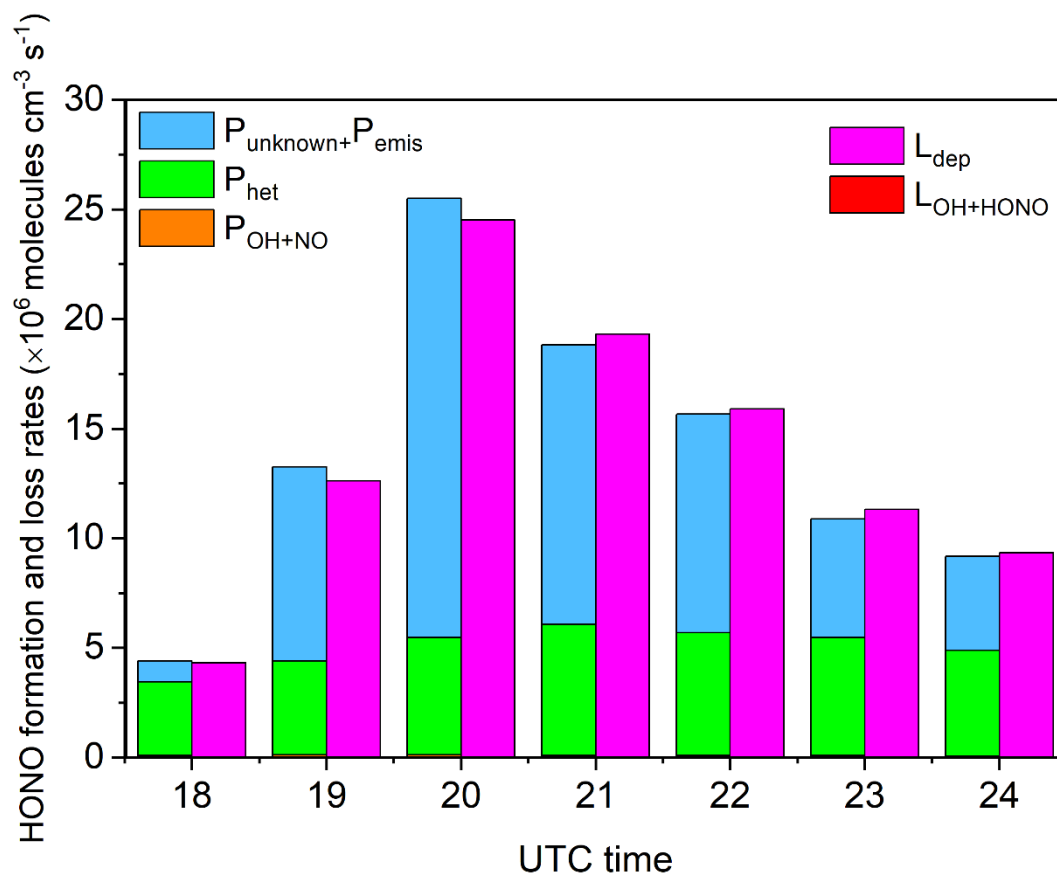


591

592 Figure 3. (A) The average steady-state OH concentration and (B) production rates from photolysis

593 of HONO and O<sub>3</sub>, and alkene ozonolysis below the forest canopy during the measurement period.

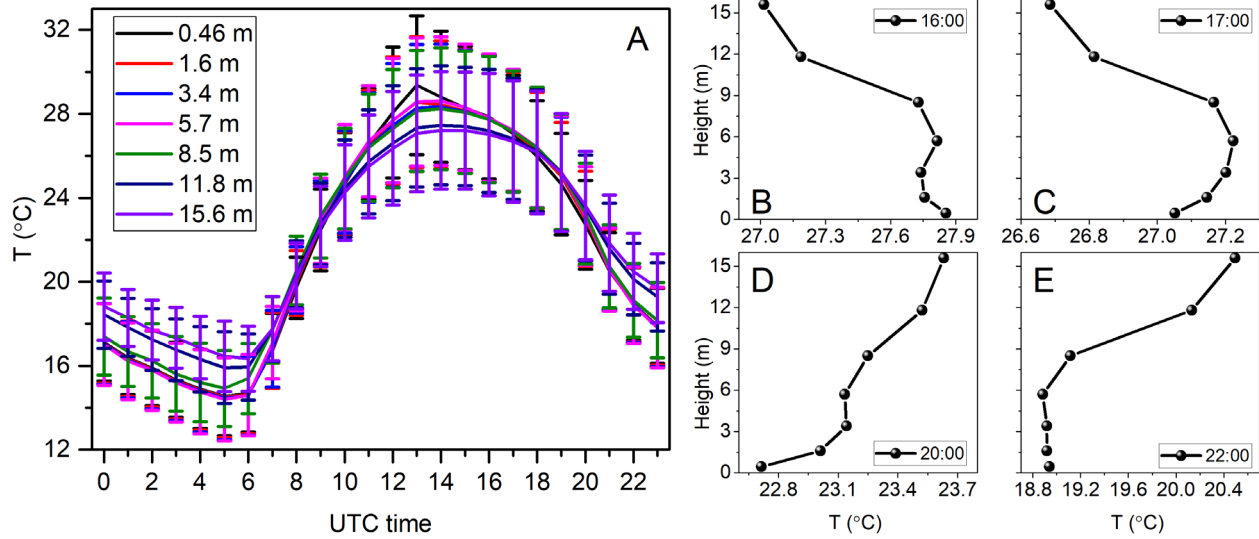
594



595

596 Figure 4. HONO formation and loss rates from different pathways during the measurement period  
597 from 5<sup>th</sup> to 25<sup>th</sup> July, 2018.

598



599

600 Figure 5. (A) Diurnal variations of vertical temperature and (B-E) the vertical average temperature  
 601 at a specific time.